Monitoring and Analysis of Surface Deformation and Glacier Motion Along the Sichuan–Tibet Railway: A Case Study of the Lhasa–Nyingchi Railway Section

Jinghui Luo, Qing Ding, Gong Zhang, Wei Zhang, Xiaoxia Wang, and Changli Zheng

Abstract The Sichuan–Tibet Railway which stretches as far as 1600 km starts from Chengdu in Sichuan Province and west to Lhasa in the Tibet Autonomous Region. The terrain along the railway is undulating, the ecological environment is fragile, and the railway passes through high-intensity active seismic belts and geological fault zones, facing a variety of geological disaster risks. Keeping abreast of changes in surface morphology along the railway and further monitoring and early warning of disasters can provide important technical support for the smooth construction and safe operation of the Sichuan–Tibet Railway. Taking the Lhasa to Nyingchi Railway section as an example, using the spaceborne SAR data, the surface deformation information along the railway was extracted by using the interferometry point target analysis (IPTA) technology, and the glacier motion information was derived by using the pixel offset-tracking (POT) technology. The observation results showed that the annual subsidence velocity was small in most areas of our study area, except the local areas along the LinMao Highway, whose subsidence velocity was more than 3.5 cm/year, which can be served as a key monitoring area. Another observation was that the velocity of glacier motion had a great relationship with the temperature change in our study area. As a whole, the velocity of glacier motion increases with the increase of temperature, and the glacier motion velocity in summer is significantly higher than that in winter. In addition, local topographic conditions such as slope and aspect also had a great influence on the glacier motion velocity of the glacier. Therefore, it is necessary to analyze the glacier motion in combination with local topographic.

Keywords Sichuan-Tibet railway · Deformation monitoring · Glacier motion · IPTA · POT

J. Luo (✉) · Q. Ding · G. Zhang · W. Zhang · X. Wang · C. Zheng
Science and Technology on Electronic Information Control Laboratory, Chengdu, China
e-mail: wsljh555@163.com

1   Introduction

The Sichuan–Tibet Railway starts from Chengdu in Sichuan Province in the east and Lhasa in the Tibet Autonomous Region in the west. It is a key line for the country to implement the "One Belt, One Road" development strategy. The planning and construction of the Sichuan–Tibet Railway have great and far-reaching significance for the long-term stability of China and the economic construction and development of Tibet. The construction of the Sichuan–Tibet Railway faces many challenges such as large terrain differences, strong seismic activity along the route and frequent mountain disasters. And it will face enormous challenges to ensure the smooth construction and future safe operation of the Sichuan–Tibet Railway in the future.

Interferometric Synthetic Aperture Radar (InSAR) technology provides the capability to monitor precise surface displacements over time with a wide coverage in a time-efficient manner [1]. It has been used successfully in various applications and fields of research as surface deformation monitoring [2], earthquake and plate movement [3, 4], infrastructure deformation [5], glacial drift [6, 7], landslide [8] and other fields. This paper takes the Lhasa–Nyingchi Railway section as an example to carry out monitoring and analysis of geological disasters along the railway, which is under construction and is also an important part of the Sichuan–Tibet Railway. We focused on surface time series deformation monitoring and glacier motion monitoring along the railway, which can provide a scientific and accurate basis for quantitative evaluation of potential geological disasters along the railway.

2   Methods

2.1   Surface Deformation Monitoring

Persistent Scatters InSAR (PS-InSAR) technology was proposed by Italian scholar Ferretti et al. [9, 10], extracting deformation information by using various ground object targets with strong backscattering of radar waves and stable timing. It inherits the advantages including wide range and high spatial resolution of differential SAR interferometry (D-InSAR) and overcomes the time and baseline miscorrelation of traditional D-InSAR. To solve the problem that the traditional PS-InSAR method can only select a small number of stable phase points (Persistent Scatters, PS) in low coherence regions, a method called interferometry point target analysis (IPTA) was developed on the basis of PS-InSAR. IPTA method only performs time dimension and space dimension analysis on extracted points to obtain large-scale surface deformation of long time series. The processing flow of IPTA is shown in Fig. 1. Taking there is only a single reference image as an example, the main technical ideas are as follows.

It is assumed that there are N SAR images of different phases in the study area, and one of them is selected as the reference image, and the remaining N-1 images are the
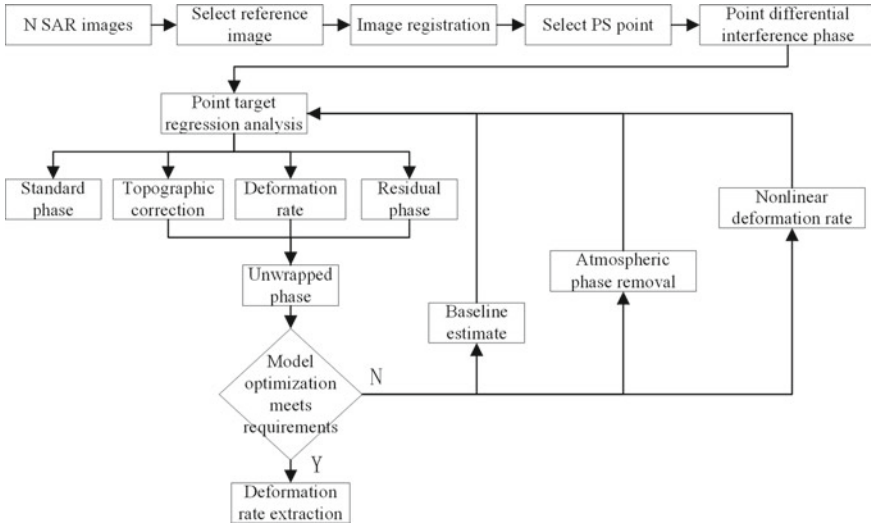
Fig. 1 Flowchart of IPTA method

slave images, which are, respectively, registered with the reference image to obtain N-1 interference pairs. By using the external DEM data and performing differential interference processing, N-1 differential interferograms can be obtained, thereby obtaining N-1 time series differential interference phases at each PS point. Then, using the regression analysis method, the elevation error and surface deformation of the PS point are obtained. The phase model of the IPTA method can be expressed as follows:

$$\varphi_{unw} = \varphi_{topo} + \varphi_{def} + \varphi_{atmos} + \varphi_{noise} \tag{1}$$

where φ_{unw}, φ_{topo}, φ_{def}, φ_{atmos} and φ_{noise} denote unwrapped interference phase of PS point, topographic error, the phase components along the radar line of sight (LOS) due to surface deformation, atmospheric artifacts and decorrelation/thermal noise, respectively. Equation (1) can also be expressed as follows using the observed geometric parameters:

$$\varphi_{unw} = \frac{4\pi}{\lambda R} \cdot \frac{B_\perp}{\sin \theta} \cdot \Delta h + \frac{4\pi}{\lambda} \cdot v \cdot T_i + \varphi_{res} \tag{2}$$

where λ, R, θ, $B_\perp$, T_i, Δh denote radar wavelength, the slant distance between radar and the ground target, radar incident angle, time baseline of interference pairs, vertical baseline of interference pairs, topographic correction, respectively. v is linear deformation rate in the LOS direction. And φ_{res} is the residual phase of the PS point including the atmospheric delay phase, the nonlinear deformation phase and the noise phase.

2.2   Glacier Motion Monitoring

The pixel offset-tracking technique uses the intensity tracking method [11] or the coherence tracking method [12] to register the two SAR images pixel by pixel and then estimates the surface displacement from the registration offset. This paper monitors the glacier motion based on the intensity tracking method, considering the POT method is more suitable for areas with low coherence and obvious surface features. The processing flow of the POT technology is shown in Fig. 2. The speckle noise information was used to perform normalized cross-correlation calculation on the intensity information of SAR images to obtain offsets between pixels, where the correlation coefficient was calculated as follows:

$$cc(x, y) = \frac{\sum_{x,y}(r(x, y) - u_r)(s(x - u, y - v) - u_s)}{\sqrt{\sum_{x,y}(r(x, y) - u_r)^2 \sum_{x,y}(s(x - u, y - v) - u_s)^2}} \tag{3}$$

where $cc(x, y)$ is normalized cross-correlation. (x, y) and $(x - u, y - v)$ represent pixel locations in reference image and slave image, respectively. r and s denote pixel values in reference image and slave image, respectively. u_r and u_s are the average pixel values in reference window and search window, respectively.
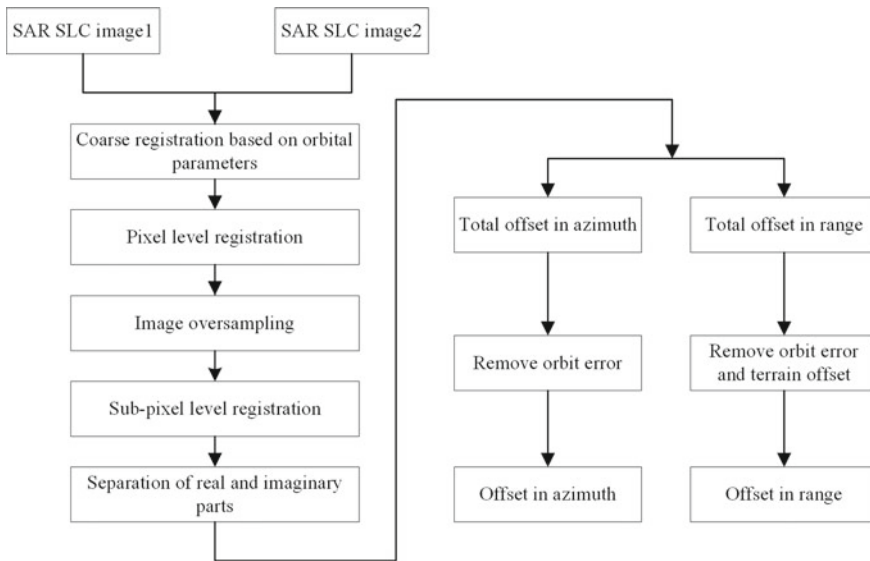

Fig. 2 Flowchart of POT method

3 Study Sites and Data

The research area of this paper is along the line of Lhasa–Nyingchi Railway and its surrounding area, N29°0′–N29°55′, E93°42′–E95°18′, mainly involving the part of Bayi district and Mainling County of Nyingchi City (Fig. 3). The red color box in Fig. 3 shows the surface deformation research area, covering a range of about 32 km × 50 km, mainly including the Lhasa–Nyingchi Railway construction section, Nyingchi Mainling Airport and other areas. The blue color box in Fig. 3 shows the glacier motion research area, covering a range of about 28 km × 30 km, with glaciers and frozen soils in the area.

The image data used to extract the surface deformation of the study area is the Sentinel-1 interference wide-mode SAR image. All images are in single-view complex format data, the incident angle is about 44°, the polarization mode is VV, the azimuth sampling interval is 20 m, and the sampling interval is 5 m. The PS candidate point targets were extracted according to the spectral characteristics and backscattering characteristics of the coherence point in the study area. When generating the differential interferogram, we selected multiple reference images, set the time baseline (Delta_T) threshold to 100 days, and the perpendicular baseline (Bperp) threshold to 200 m. Then, we got a total of 87 interference image pairs. After eliminating the poor quality interference pairs, we finally got 61 high-quality interference pairs (Fig. 4). In Fig. 4, the axis of abscissa represents the image acquisition time, and the axis of ordinate represents perpendicular baseline. The number 1–31 in Fig. 4 corresponds to the 31 images at 12 days interval between September 5, 2017 and August 31, 2018.
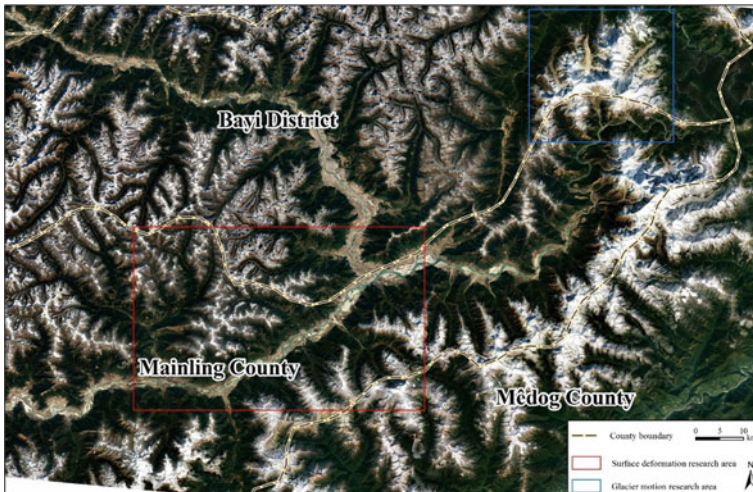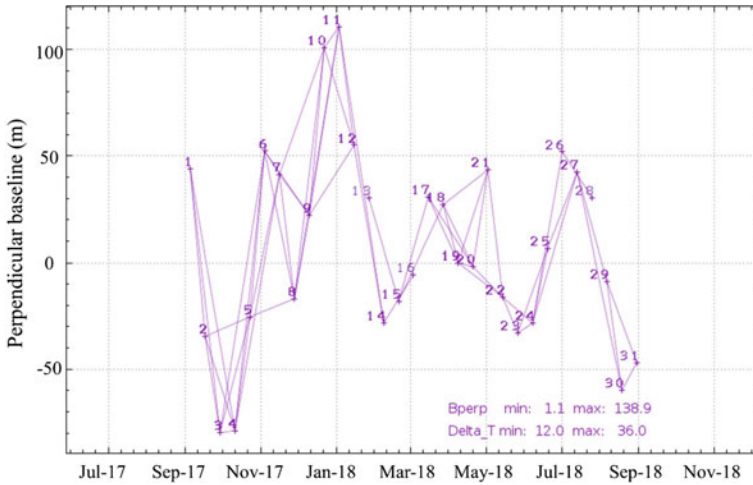

Fig. 3 Range of study area

**Fig. 4** High-quality interferometry pairs

Table 1 Details of image pairs

Orbit	No.	Reference image	Slave image	Delta_T/d	Bperp/m	Mode
1	1	20170614	20171101	140	−85.3	Fine
	2	20171101	20180307	126	484.2	Fine
2	3	20170706	20171109	126	332.8	Fine
	4	20171109	20180510	182	−128.0	Fine

Image data used for dynamic monitoring of glacier motion is ALOS-2 strip mode data. The image acquisition time is from 2017 to 2018, with a total of six scene images, distributed in two orbits (satellites in orbital 1 and orbit 2 have opposite directions of flight, the orbital 1 has an incident angle of about 41°, and the orbital 2 has an incident angle of about 31°). The image has a width of 70 km and an azimuth sampling interval of 3.2 m. Image information and combinations are shown in Table 1.

4 Results and Discussion

4.1 IPTA

The PS-InSAR results along the Lhasa–Nyingchi Railway section and its surrounding areas are shown in Fig. 5. The name of the county, major roads and some locations are marked in figure. The deformation velocity range is set to −3.5 to 3.5 cm/y. In
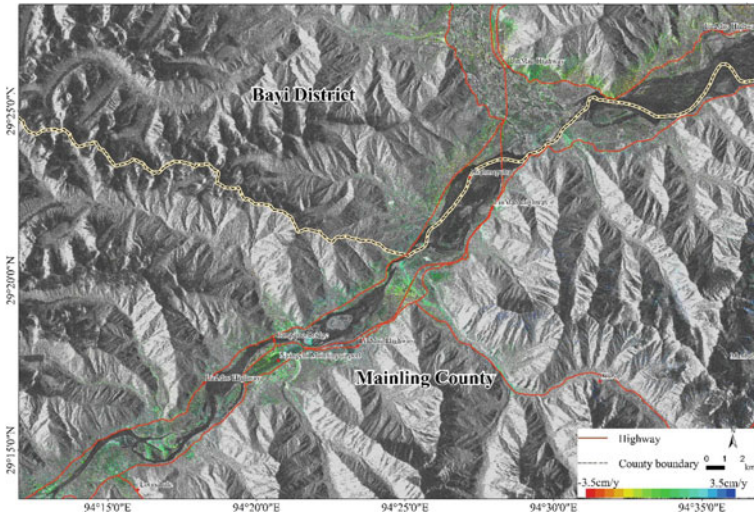
Fig. 5 Deformation velocity map

this study, we only care about the deformation information along the railway and the surrounding area. Therefore, most of the mountainous areas are masked, and the deformation velocity maps of relevant areas are not shown the figure.

It can be seen from Fig. 5 that during the period from September 5, 2017 to August 31, 2018, the annual deformation of most areas in the study area was small, and only a small part area has a large deformation. The ground subsidence was mainly concentrated along the LinMao Highway in the northeast of velocity map. The local deformation was more than 3.5 cm/year, which can be served as a key monitoring area.

Ground uplift mainly occurs in the northeastern part of Nyingchi Mainling Airport, where there was an overall uptrend. This condition may be related to the changes of flood season and dry season of the Brahmaputra River. In the summer (July, August and September), the Brahmaputra River was in its flood season, the water volume increased and flooded some of the tidal flats and coastal areas. In other seasons, river water volume decreased, and some flooded areas appeared.

4.2   POT

The dynamic monitoring results of glacier motion are shown in Figs. 6, 7, 8 and 9. The slope and aspect distributions of the corresponding study area are shown in Fig. 10, which were extracted from the SRTM DEM data of 30 m resolution. Figures 6, 7, 8 and 9 represent the motion velocity maps of different time periods derived from ALOS-2 data. Each color cycle in the figures represents a motion rate of 60 cm/d.
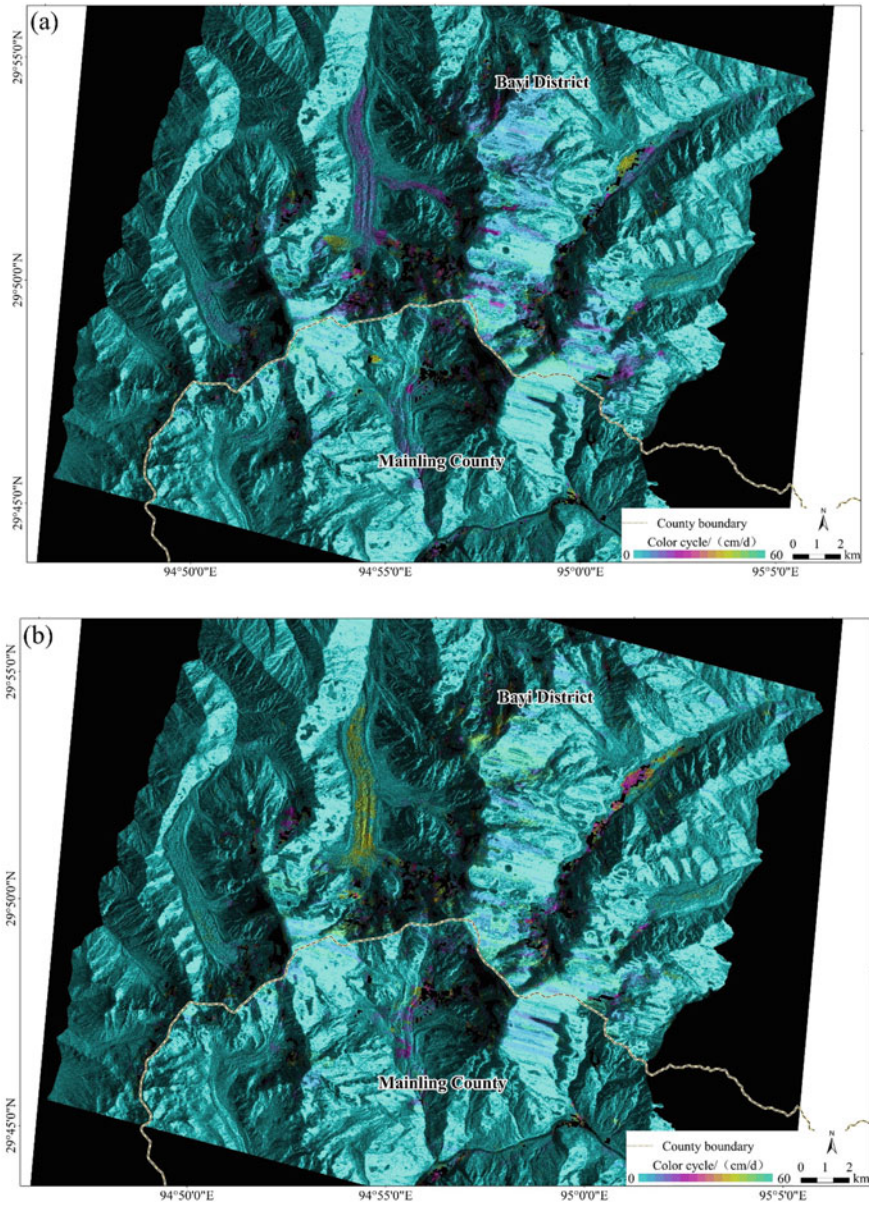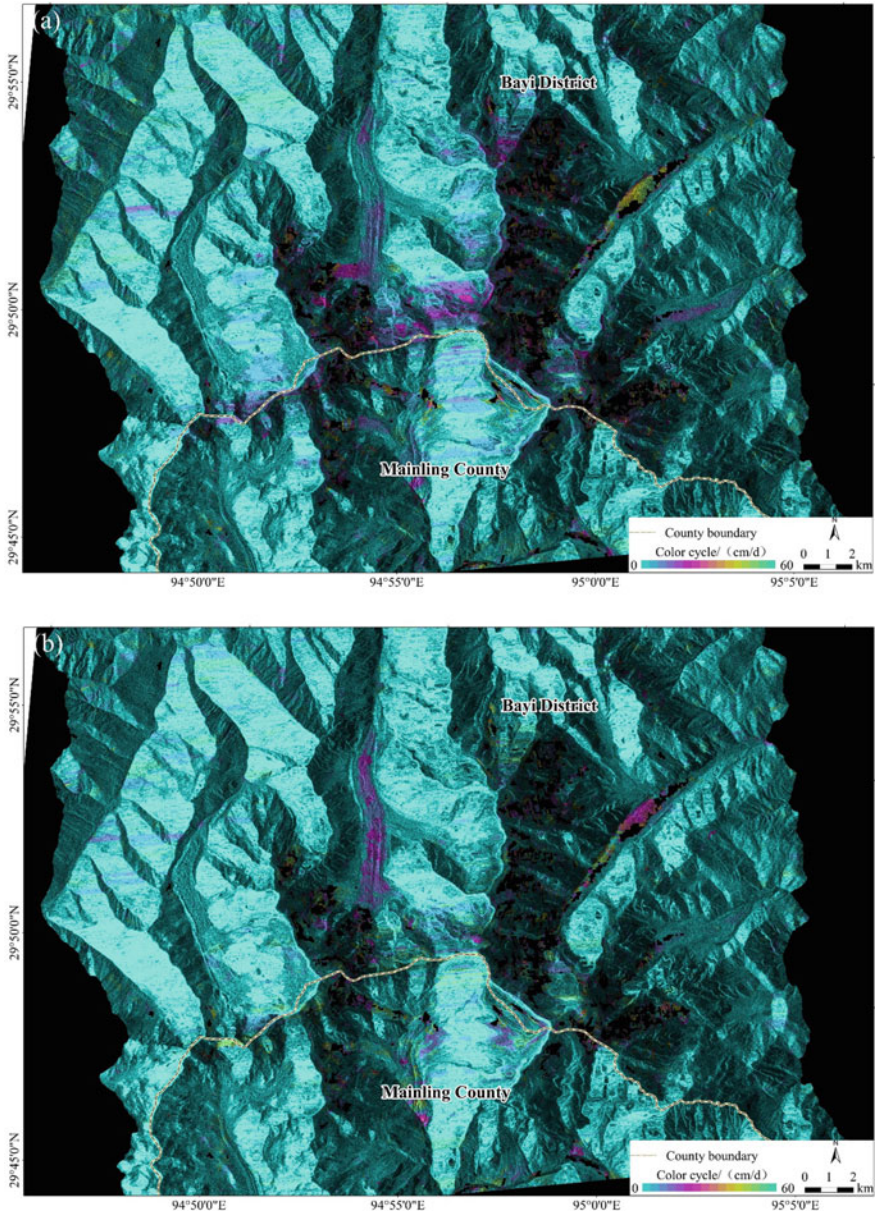
Fig. 6 Motion velocity maps of glacier from image pair 20170614–20171101. **a** In range; **b** in azimuth
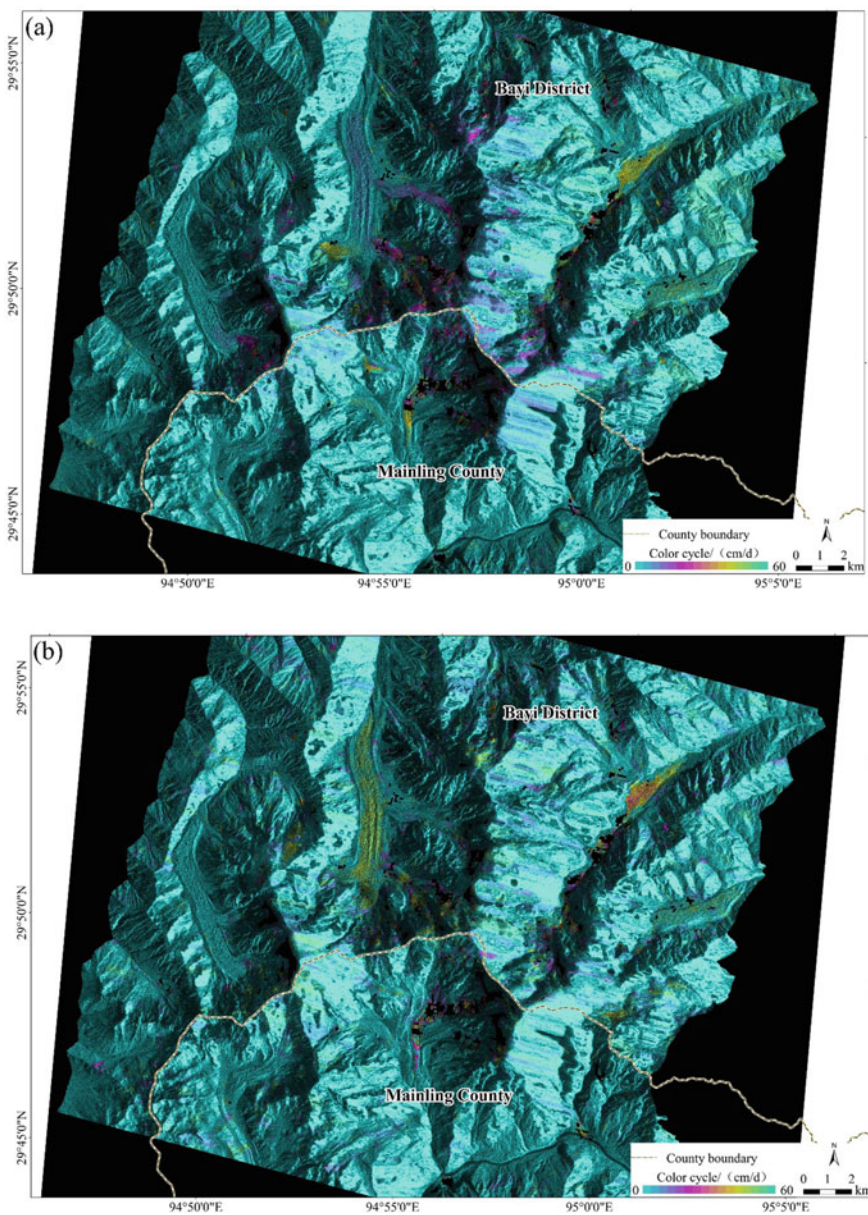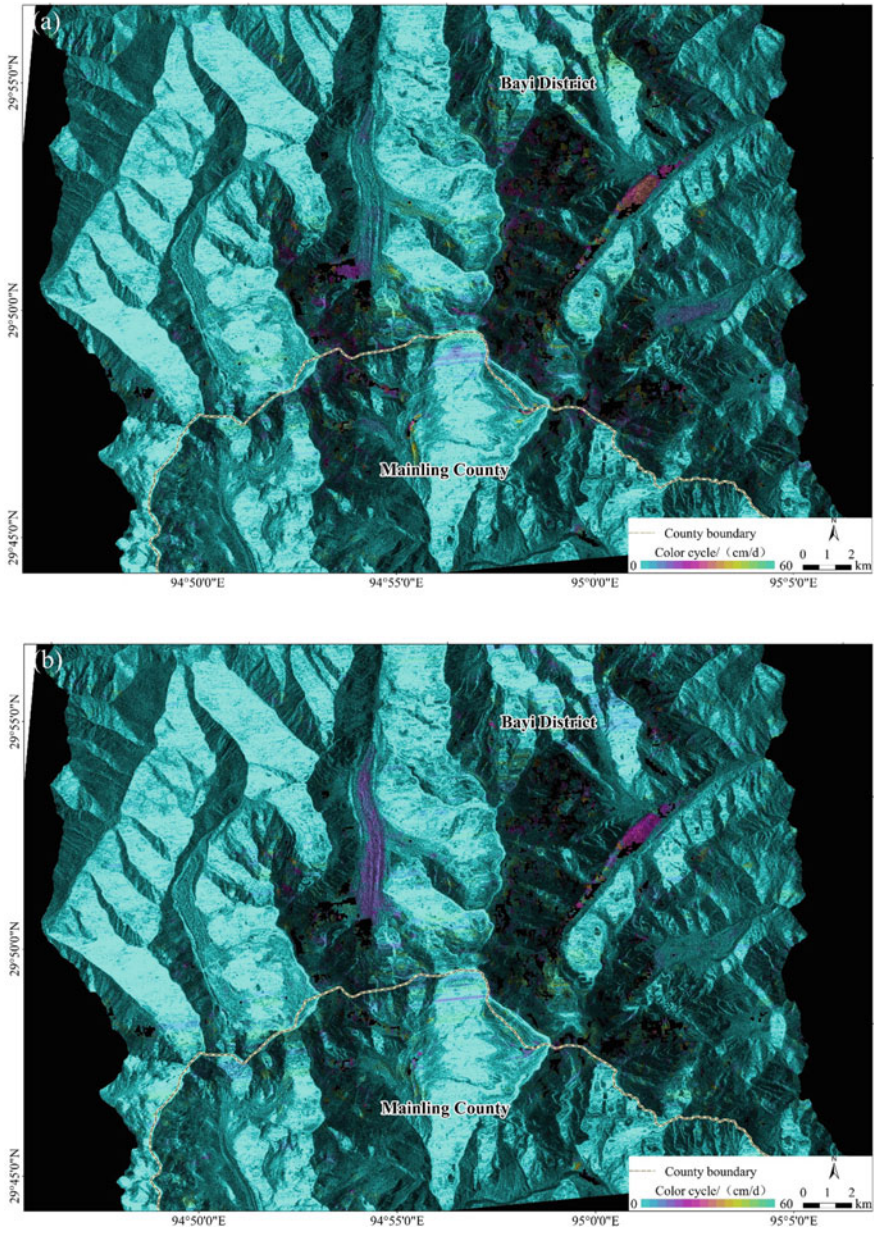
Fig. 7 Motion velocity maps of glacier from image pair 20171101–20180307. **a** In range; **b** in azimuth
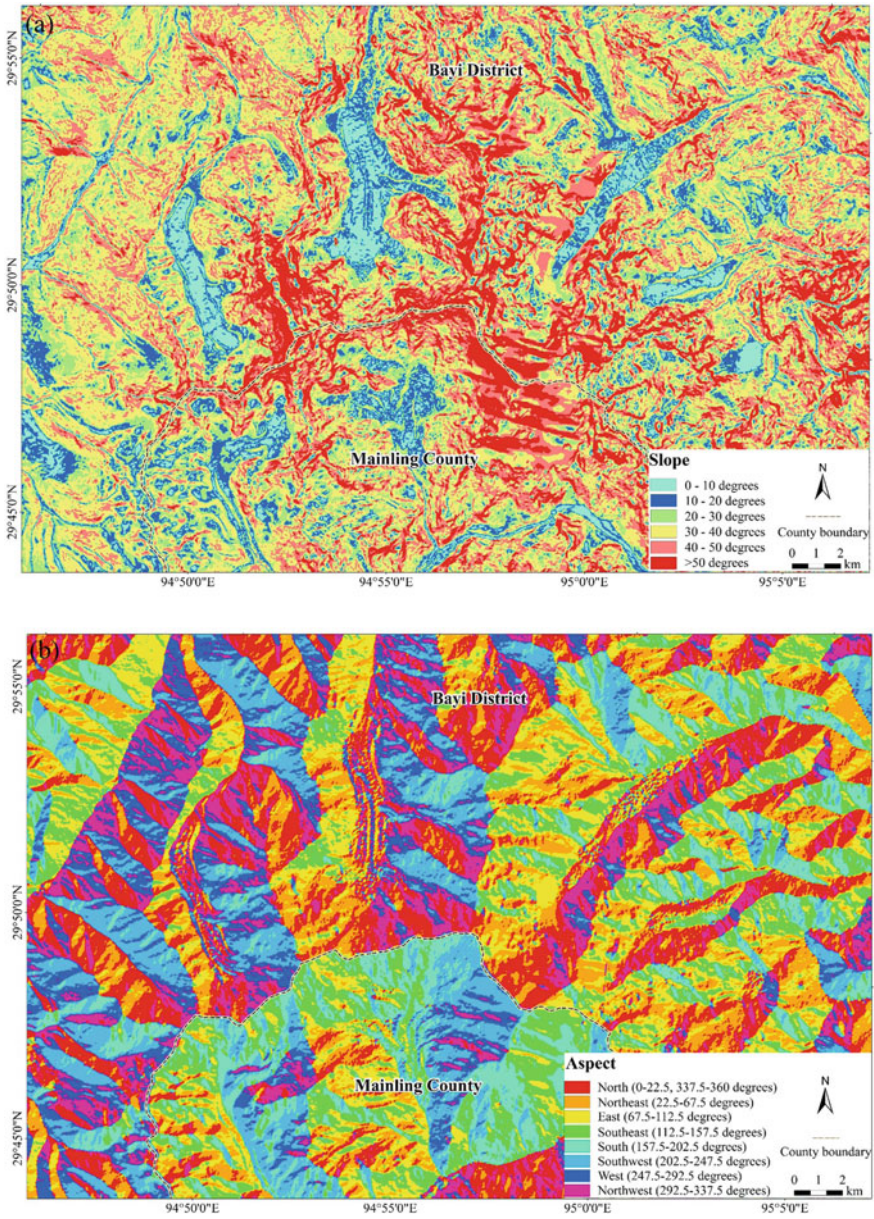
Fig. 8 Motion velocity maps of glacier from image pair 20170706–20171109. **a** In range; **b** in azimuth

Fig. 9 Motion velocity maps of glacier from image pair 20171109–20180510. **a** In range; **b** in azimuth

Fig. 10 Slope and aspect distribution maps of study area. **a** Slope; **b** aspect

There were some black areas in the effective data range of the study area, which are low correlation areas and SAR imaging overlap shadow areas. In addition, due to natural phenomena such as wind, rain and snow, the scattering characteristics of the target may have changed, resulting in registration accuracy in some areas. It also caused empty values and motion rate mutation points in some areas.

The results show that the motion velocity of the glacier has a great relationship with the temperature change. As the summer temperature rises, the speed of glacier movement increases, and the velocity of glaciers in summer is significantly faster than that in winter. Reflected in the figure, the velocity of glacier motion in 20170614–20171101 period (Fig. 6) is faster than that in 20171101–20180307 period (Fig. 7) of orbit 1; the velocity of glacier motion in 20170706–20171109 period (Fig. 8) is faster than that in 20171109–20180510 period (Fig. 9) of orbit 2; the flow rate of the glaciers in 20171109–20180510 period of orbit 1 is significantly increased compared with 20171101–20180307 period of orbit 2, which is consistent with the increase of glacier flow rate with increasing temperature. At the same time, we also noticed that the derived glacial motion velocity defers by using SAR data acquired in different orbits at the same time period. It is obviously that the glacier motion velocity in Fig. 6 is about 10 cm/d faster than that in Fig. 8. The main difference is that the satellite heading and incidence angle of the two orbits are different. In complex mountainous terrain conditions, the range of data obtained by the two orbits varies.

Local topographic also has a large impact on the flow rate of the glacier. The satellite flies in the north–south direction in both orbit 1 and orbit 2, but orbit 1 is an ascending orbit, and orbit 2 is the opposite. As shown in Figs. 6, 7, 8 and 9, the glacier motion velocity varies greatly in range and in azimuth. In the figures, the north–south flowing glaciers have a smaller motion velocity in range than that in azimuth. And the east–west flowing glaciers have a smaller velocity of motion in azimuth than that in range. Take the north–south flowing glacier that in the middle of the figures as an example, considering the data of which is relatively complete. We can find that from the upper part of the glacier to the end of the ice tongue, the motion velocity of the glacier increases first and then decreases gradually. The flow velocity of the glacier is less than the middle on both sides, and the velocity at the end of the ice tongue is obviously slowed down. From Fig. 10, we can find that the glacier slope is generally northward, the glacier slope is mostly between 0° and 20°, and the glacier slope in middle is slightly higher than that in the two sides. This also confirms that the glacier velocity we found is affected by local topographic.

In addition, the glacier surface and bottom dam will also affect the motion velocity of glaciers. Even in different glaciers or different glaciers in the same area, the glacier motion velocity may be different. Therefore, specific analysis is needed for specific study areas to quantitatively evaluate their potential disaster risks and hazards.

5   Conclusions

Taking the Lhasa–Nyingchi Railway section as an example, this paper used PS-InSAR technology to extract the surface time series deformation information along the railway on the basis of spaceborne SAR data. In addition, considering that there are many glacial groups along the Sichuan–Tibet Railway, with global warming, glaciers melting accelerated, and there is a potential risk of geological disasters. Therefore, POT technology was used to extract the glacier motion velocity and dynamically monitor the evolution of glaciers. The results showed that SAR interferometry technology can be used for surface deformation and glacier motion monitoring, thus can provide important technical support for disaster monitoring and early warning. It should be pointed out that due to the limitation of data, the monitoring results were not verified in this paper. Next, we will apply for the leveling surveying data in similar periods from relevant departments to calibrate and verify our PS-InSAR and POT monitoring results.

References

1. Tazio S, Frank P, Andreas W et al (2017) Circum-Arctic changes in the flow of glaciers and ice caps from satellite SAR data between the 1990s and 2017. Remote Sens 9(9):947
2. Zhang Y, Zhang J, Gong W et al (2009) Monitoring urban subsidence based on SAR interferometric point target analysis. Acta Geod Cartogr Sin 38(6):482–487
3. Ji L, Liu C, Xu J et al (2017) InSAR observation and inversion of the seismogenic fault for the 2017 Jiuzhaigou Ms 7.0 earthquake in China. Chin J Geophys 10:4069–4082
4. Jiang M, Ding X, Li Z et al (2009) Study on coseismic deformation of WenChuan earthquake by use of L and C wavebands of SAR data. J Geod Geodyn 29(1):21–26
5. Qin X, Yang M, Wang H et al (2016) Application of high-resolution PS-InSAR in deformation characteristics probe of urban rail transit. Acta Geod Cartogr Sin 45(6):713–721
6. Li J, Li Z, Wang C et al (2013) Using SAR offset-tracking approach to estimate surface motion of the South Inylchek Glacier in Tianshan. Chin J Geophys 56(4):1226–1236
7. Wang X, Liu Q, Jiang L et al (2015) Characteristics and influence factors of glacier surface flow velocity in the Everest region, the Himalayas derived from ALOS/PALSAR images. J Glaciol Geocryol 37(3):570–579
8. Li Z, Song C, Yu C et al (2019) Application of satellite radar remote sensing to landslide detection and monitoring: challenges an solutions. Geomatics Inf Sci Wuhan Univ 44(7):967–979
9. Ferretti A, Prati C, Rocca F (2001) Permanent scatterers in SAR interferometry. IEEE Trans Geosci Remote Sens 39(1):1–20
10. Ferretti A, Fumagalli A, Novali F et al (2011) A new algorithm for processing interferometric data-stacks: SqueeSAR. IEEE Trans Geosci Remote Sens 49(9):3460–3470

11. Rott H, Stuefer M, Siegel A et al (1998) Mass fluxes and dynamics of Moreno Glacier, Southern Patagonia Icefield. Geophys Res Lett 25(9):1407–1410
12. Pattyn F, Derauw D (2002) Ice-dynamic conditions of Shirase Glacier, Antarctica, inferred from ERS SAR interferometry. J Glaciol 48(163):559–565